

Deep Learning-Based Annotation Transfer between Molecular Imaging Modalities: An Automated Workflow for Multimodal Data Integration

Alan M. Race,* Daniel Sutton, Gregory Hamm, Gareth Maglenon, Jennifer P. Morton, Nicole Strittmatter, Andrew Campbell, Owen J. Sansom, Yinhai Wang, Simon T. Barry, Zoltan Takáts, Richard J. A. Goodwin, and Josephine Bunch



Cite This: *Anal. Chem.* 2021, 93, 3061–3071



Read Online

ACCESS |

Metrics & More

Article Recommendations

Supporting Information

ABSTRACT: An ever-increasing array of imaging technologies are being used in the study of complex biological samples, each of which provides complementary, occasionally overlapping information at different length scales and spatial resolutions. It is important to understand the information provided by one technique in the context of the other to achieve a more holistic overview of such complex samples. One way to achieve this is to use annotations from one modality to investigate additional modalities. For microscopy-based techniques, these annotations could be manually generated using digital pathology software or automatically generated by machine learning (including deep learning) methods. Here, we present a generic method for using annotations from one microscopy modality to extract information from complementary modalities. We also present a fast, general, multimodal registration workflow [evaluated on multiple mass spectrometry imaging (MSI) modalities, matrix-assisted laser desorption/ionization, desorption electrospray ionization, and rapid evaporative ionization mass spectrometry] for automatic alignment of complex data sets, demonstrating an order of magnitude speed-up compared to previously published work. To demonstrate the power of the annotation transfer and multimodal registration workflows, we combine MSI, histological staining (such as hematoxylin and eosin), and deep learning (automatic annotation of histology images) to investigate a pancreatic cancer mouse model. Neoplastic pancreatic tissue regions, which were histologically indistinguishable from one another, were observed to be metabolically different. We demonstrate the use of the proposed methods to better understand tumor heterogeneity and the tumor microenvironment by transferring machine learning results freely between the two modalities.



INTRODUCTION

No single technique can provide all necessary information to comprehensively investigate complex biological samples. In the study of cancer, a wide range of imaging techniques are used at the various stages of research.¹ Traditional imaging methodologies which allow visualization of tissue morphology (heterogeneity), proteins, and fluorescent biomarkers with high specificity and spatial resolution, such as hematoxylin and eosin (H&E) staining (and more broadly, immunohistochemical staining) and fluorescence microscopy, are targeted and therefore require prior knowledge.² More recently, mass spectrometry imaging (MSI) has been increasingly applied in oncology and pharmacology as it provides means to identify and map the distribution of both exogenous and endogenous molecules simultaneously in a label-free manner.³ It is however important to consider MSI data in the context of histology data. Through the integration of these modalities, it is possible to gain more insights into the underlying biology.⁴

Chaurand et al. demonstrated the first application of MSI and histology staining on the same section, with MSI being

performed on already stained sections.⁵ In the years since, it has become common practice to perform MSI and histology on the same section (albeit typically with staining following the MSI) or on an adjacent section depending on the destructiveness of the ionization probe.⁶

As both modalities provide complementary information, it is desirable to integrate the resulting images to enable a more comprehensive understanding of the data. This requires image registration to be performed, which is the process of aligning the two images such that the same biological features in each modality overlap one another. This process is not trivial as it must account for potentially large differences in pixel sizes between the two modalities, shearing and rotation introduced

Received: June 26, 2020

Accepted: January 22, 2021

Published: February 3, 2021



through differences in sample holders or instrument geometries, and also differences in tissue shape when using sequential tissue sections (such as different visible features as a function of depth, tearing, and folding). Registration of MSI and histology data remains an active area of research, with a number of solutions proposed, which are often tailored to specific experimental setups (e.g., the use of laser ablation craters for alignment excludes its use for techniques without a laser).^{7–9}

Once the data are aligned, new data integration workflows become possible. Heijs et al. and Patterson et al. used annotated histology to dictate where high-resolution matrix-assisted laser desorption/ionization (MALDI) MSI data should be acquired, albeit with different registration workflows.^{9,10} Verbeeck et al. registered histology images to a reference brain atlas to interpret MSI data in the context of brain anatomy.¹¹ Dewez et al. used annotated histology and clustering applied to MSI data to automatically extract regions using laser capture microdissection for subsequent microproteomics.¹²

Most of these new workflows rely on annotated histology data to distinguish regions with morphological or biological differences, which are then used for subsequent analysis. Previous work has enlisted the help of expert pathologists to perform such annotations. As the process to fully annotate a single section can easily take an hour (or more for complex tissues), this quickly becomes a bottleneck in large imaging studies. Recent advancements in the field of image segmentation and digital pathology have demonstrated high classification accuracy of histological images in a fraction of the time while also often exceeding the accuracy achieved by an experienced human pathologist.¹³ This is particularly true of deep learning-based algorithms which provide pixel-level classification of images.^{14,15}

For many studies, it is only through true data integration that the biological questions can be answered. To transfer annotations from one modality to another, current methods typically create an image for each annotation and then transform it to the space of the other modality. This is a comparatively computationally (and memory) intensive operation, especially for whole slide optical microscopy images which can exceed tens of billions of pixels, requiring the images to be interpolated to fit into the new space.

In this study, we present a method for integrating histology and MSI data, enabling information to be freely transferred from one modality to the other, and back again, and demonstrate its use to study the tumor microenvironment (TME) in a KPC pancreatic ductal adenocarcinoma (PDAC) mouse model.

■ EXPERIMENTAL SECTION

Animal Experiments. All animal experiments were performed under Home Office license and approved by the University of Glasgow Animal Welfare and Ethical Review Board. Mice were maintained in conventional cages and given access to standard diet and water ad libitum. KPC (LSL-Kras^{G12D/+}; LSL-Trp53^{R172H/+}; and Pdx1-Cre) mice¹⁶ were bred in house on a mixed background. Mice were genotyped by Transnetyx (Cordoba, TN, USA). Mice of both sexes were monitored at least 3 times weekly and culled when exhibiting signs of PDAC.

Tumor samples were removed at necropsy with surrounding margins to ensure complete excision. Upon removal, the tissue

was snap frozen in supercooled (−70 to −80 °C) isopentane and stored at −80 °C before use.

Mass Spectrometry Imaging. Hydroxypropyl methylcellulose (HPMC) and poly-vinylpyrrolidone (PVP) were purchased from Sigma-Aldrich (Dorset, UK). HPLC grade water and methanol were obtained from Merck (Hohenbrunn, Germany).

PDAC samples were embedded in a HPMC + PVP hydrogel to enable simultaneous and identical processing for all specimens analyzed in an experiment.¹⁷ Tumors from three animals were placed upright in Peel-A-Way molds (Thermo Scientific, Waltham, Massachusetts, USA) pre-filled with ice cold embedding medium before snap freezing in dry ice-chilled isopropanol, followed by a wash in dry ice-chilled isopentane. The frozen molds were kept on dry ice until all adherent isopentane was evaporated before further processing.

Tissue blocks were sectioned to a 10 μm thickness using a CM3050 cryo-microtome (Leica Biosystems, Nussloch, Germany), thaw-mounted onto Superfrost slides (Fisher Scientific, Loughborough, UK), and subsequently nitrogen dried before being stored at −80 °C until analysis.

Desorption electrospray ionization (DESI)-MSI was performed using an automated 2D DESI source (Prosolia Inc., Indianapolis, IN, USA) with a home-built sprayer assembly (as described by Abbassi-Ghadi et al.¹⁸) mounted to a Q-Exactive FTMS instrument (Thermo Scientific, Bremen, Germany). All images were recorded at a pixel size of 70 μm. Images were recorded in the negative ion mode using a mass range of 80–900 Da with 150 ms injection time, a mass resolving power of 70,000 at *m/z* 200, and a S-Lens setting of 75. Methanol/water (95:5 v/v) was used as the electrospray solvent at a flow rate of 1.5 μL/min, a spray voltage of −4.5 kV, and a nebulizing pressure of 6.5 bar (nitrogen N4.8). Solvent was delivered using a standalone Dionex Ultimate 3000 pump. Distance between the DESI sprayer and the MS inlet was 7 mm, and the distance from the sprayer tip to the sample surface was 1.5 mm at an angle of 75°. Individual line scans were converted into centroided mzML format using MSConvert (ProteoWizard toolbox version 3.0.4043¹⁹) and subsequently into imzML using imzMLConverter version 2.1.0.²⁰ Data were then reduced (peak detection was performed on the mean spectrum and peak intensities for each spectrum were generated by summing between peak limits) using SpectralAnalysis version 1.2.0.²¹ Data were normalized using root-mean-square normalization. All annotations are tentative identifications, assigned from exact mass only using the HMDB,²² METLIN,²³ and LIPID Maps²⁴ databases.

H&E Staining and Scanning. H&E staining was performed post DESI MSI analysis on same tissue sections. The stained sections were imaged at 40× magnification (0.226 μm/pixel) with the Aperio CS2 digital pathology scanner (Leica Biosystems) and visualized with either ImageScope software (Leica Biosystems version 12.3.2.8013) or HALO (Indica Labs v3.0.311.261).

Individual image files for each section on the whole slide were manually extracted using ImageScope to the tiff format. A custom tool was then used to ensure that the XResolution and YResolution tags in the tiff metadata matched the pixel size in the original whole slide file.

H&E Deep Learning Classification. The deep learning training regions were selected on pathologist lead annotations generated using ImageScope. Three regions were identified as being of interest: non-neoplastic pancreatic tissue, connective

tissue, and PDAC tumor regions. Non-neoplastic acinar tissue mainly comprised pyramidal zymogenic cells surrounding a central lumen. These were interspersed with interlobular ducts, intercalated ducts, and blood vessels. Connective tissue consisted of loosely organized fibroblasts embedded in collagen bundles with associated vasculature. Within the pancreas, the connective tissue projects into the gland to form septae and lobules and to serve as scaffolding for blood vessels and ducts. PDAC tumor tissue was identified as disorganized infiltrating glandular and ductal structures often associated with a desmoplastic stroma. The degree of differentiation can vary from well-formed glands to poorly oriented cells infiltrating singly or forming solid sheets.²⁵

Whole slide image (WSI) files were loaded into the HALO image analysis software (Indica Labs v3.0.311.261) running on a computer equipped with an NVIDIA Titan XP. Three training classes were created on eight WSIs (each containing 6–10 tissue sections): “tumor”, “acinar tissue”, and “connective tissue” with representative areas from each class included from the pathologist-defined regions. A DenseNet model (pretrained on the ImageNet data set²⁶) was then trained, using transfer learning, on images with pixels of maximum size 2.03 $\mu\text{m}/\text{pixel}$, to detect the large-scale tissue regions.²⁷ The model was run for over 110,000 iterations, resulting in a cross entropy of 0.055. The minimum object size was set to 10,000 μm^3 , merging smaller classified objects into the dominant surrounding classification. Tissue classifications were checked for accuracy by the pathologist to ensure concordance with the training annotations.

The white space on the slide was disregarded using a random forest algorithm, and the tissue was automatically annotated and selected for further analysis. This increased the efficiency of the DenseNet classification by excluding unnecessary pixels from analysis and provided a tissue outline annotation for the MSI images.

Multimodal Registration. The resulting classifications from the histology data were converted to a grayscale image, where pixels with the same classification were allocated the same intensity value (with 0 indicating the background, where there was no classification, and 1–3 assigned to tumor, acinar tissue, and connective tissue, respectively). This image was exported to the tiff format, incorporating the pixel size metadata (XResolution and YResolution tags). This formed the “fixed” image in the registration process.

To generate a representative image for the MSI data (the “moving” image), one of the dimensional reduction methods listed below was applied to the on-tissue spectra (with either no normalization, total ion current (TIC) normalization, or L^2 norm applied) to reduce the number of dimensions to 3 or 1. On-tissue spectra were determined using k -means clustering ($k = 3$) on the full MSI data, which provided a cluster for spectra corresponding to on-tissue, embedding medium, and glass. The central (spatially within the MSI image) cluster was then retained as the on-tissue mask. The resulting embeddings from the dimensionality reduction were then assigned to the $L^*a^*b^*$ color space to ensure that the reduced dimensions are captured in a perceptually linear manner²⁸ and then converted to RGB (red, green blue 3 channel color image) and output as a tiff file with the corresponding pixel size stored in the metadata. t-Distributed stochastic neighborhood embedding (t-SNE) was used as implemented in Scikit-learn (version 0.23.2).^{29,30} Uniform manifold approximation and projection (UMAP) were applied using the UMAP python package (version

0.4.5).³¹ Ivis was applied using the Ivis python package (version 1.8.1).³²

Image registration was performed using *elastix* version 4.9.0, with a representative tiff image from each modality and a corresponding mask image as an input.³³ Parameters for registration (denoted using exact capitalized names used by *elastix*) were as follows: MultiResolutionRegistration performed with four resolutions (8, 4, 2, and 1) with 32 histogram bins to find an AffineTransform using the AdaptiveStochasticGradientDescent to optimize for AdvancedMattesMutualInformation. Maximum of 500 iterations was performed with random sampling (with 2000 samples per iteration). Histology images were used as the fixed image and MSI images as the moving image.

Annotation Transfer. A single annotation (e.g., tumor) can consist of multiple areas of the image (polygons). Each area can also contain holes (parts of the polygon that do not form part of the annotation). Each polygon (and hole) is defined by a series of coordinates (pixel indices), each of which is a vertex of the polygon (or hole). An annotation file contains one or more annotations and is typically stored in XML (as is the case for both HALO AI and ImageScope). Regions of interest (ROI) files (.roi; pixel coordinates for each pixel that form part of the ROI are stored), generated from MSI data using either clustering or classification (as below), were output using SpectralAnalysis.²¹

The output from *elastix* (described in “**Multimodal Registration**” section) was used to construct a transformation matrix, which was then used to transfer each coordinate in either the annotation or ROI file into the space of the other modality. Details of how this is performed can be found in the **Supporting Information**.

Transferred annotations from MSI were output in XML annotation files compatible with digital pathology software such as HALO and ImageScope for visualization. Transferred annotations from optical data were output as .roi files compatible with SpectralAnalysis for interrogation of MSI data.

MSI data were extracted based on the deep learning annotations transferred from H&E to MSI ROI using SpectralAnalysis.²¹ k -means was applied to the reduced MSI data set using cosine as a distance metric and five replicates. A k -nearest-neighbor (KNN) classification model was learnt using cosine as a distance metric and 20 nearest neighbors, with the transferred annotations forming the labels for each spectrum.

RESULTS AND DISCUSSION

Traditional annotation of histological images into distinct classes (e.g., tumor and connective tissue) is performed by a trained pathologist. For a single section from the PDAC mouse model used in this study, this took approximately 1 h. For studies that require annotation of multiple technical replicates (serial sections analyzed in the same way) and multiple biological replicates (e.g., different mice which have been treated in the same way) for multiple treatment conditions, this quickly becomes infeasible.

Machine learning, in particular deep learning, is increasingly being used to automatically perform image classification and segmentation tasks, with accuracy comparable to trained experts.³⁴ Deep learning requires large amounts of labeled images to learn successful models. Such biomedical data sets are rare, and so, to take advantage of deep learning to classify histology images, transfer learning can be employed. Transfer

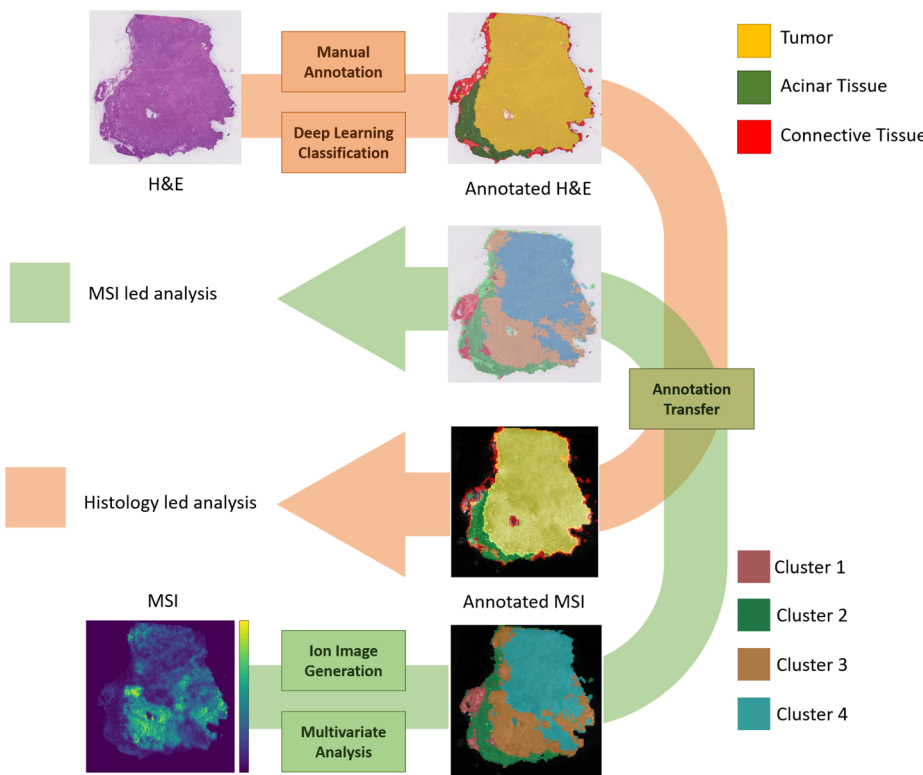


Figure 1. Annotation transfer workflow, demonstrating translation of annotations from one modality to another (and optionally back again). The workflow is agnostic to the means of creating annotations and the registration method used.

learning uses a model, pretrained on non-domain-specific data (e.g., the ImageNet database²⁶) to learn general distinguishing features, which is then fine-tuned on a smaller amount of domain-specific data.^{34,35}

Following training of the deep learning (DenseNet) model (5 h) to differentiate tumor, acinar tissue, and connective tissue classes in the H&E-stained sections, the classification of a single section took just 2 min. The training progress at various iteration milestones is shown in Figure S1 with representative images of each class, as shown in Figure S10. As the training is only performed once per model (where the model describes how the different classes are differentiated for this specific histological stain and sample-type combination) and does not require any interaction during this time, its time cost is largely insignificant. However, the introduction of a new class, splitting or merging of existing classes, or application to a new histological stain or mouse model would require retraining of the model.

To gain more insights into the underlying biology, such histological annotations can be used to interpret MSI data.⁴ The proposed annotation transfer workflow enables annotations to be freely transferred between MSI and histology data (as shown in Figure 1). The workflow can use any combination of annotations generated manually by machine learning models from user-friendly software or from custom-built state-of-the-art architectures and algorithms. However, before these annotations can be used within (or transferred to) another modality, a mapping between the two modalities must be determined. This can be achieved through multimodal image registration.

Registration. To perform image registration using algorithms and software developed in other fields, such as *elastix*,³³ representative images must be selected, which

highlight features present in both modalities. These features can be either intentionally incorporated, such as the use of fiducial markers,³⁶ or aspects of the sample visible in both modalities. The registration process itself is separate from the selection of representative images and can either be performed manually (where an expert selects matching control points in both modalities) or by using automated methods (which search for the optimal transformation to reduce some overlapping information criterion).³³

Recently, Patterson et al. proposed methods for registering data from the same section, which makes use of the laser ablation marks in MALDI, in addition to autofluorescence microscopy, to accurately align MSI and post-MSI histology.^{8,9} These methods are only applicable to techniques, which leave individual, distinct marks in the sample and would therefore not be suitable for any technique which rasters across the sample, does not leave visible marks, or is destructive. Such techniques include certain MALDI instruments and DESI used in this study, rapid evaporative ionization mass spectrometry (REIMS), secondary ion mass spectrometry, laser ablation inductively coupled plasma mass spectrometry, and imaging mass cytometry (IMC).

A more general workflow was proposed by Abdelmoula et al.³⁷ to register data from either the same section or serial sections. In this method, a representative image of the MSI data is generated using t-SNE to reduce the MSI data to three dimensions, which is then converted to a grayscale image (reducing further to one dimension). This grayscale image is then registered to histology using *elastix* with mutual information as a metric for determining optimal alignment. While this method can produce accurate results, it has drawbacks affecting its use more generally that are addressed below.

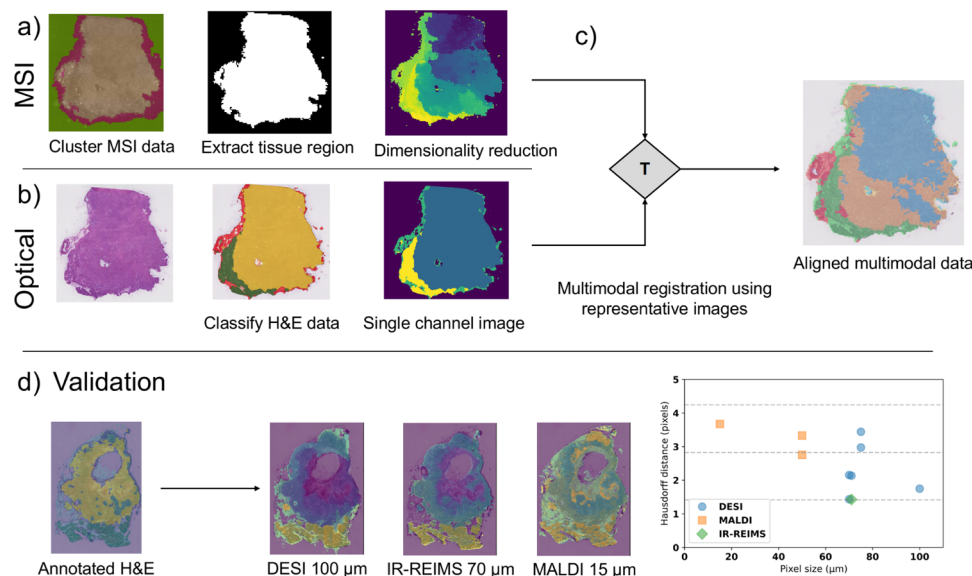


Figure 2. General multimodal image registration workflow using representative images from each modality and masks to perform the alignment. (a) MSI representative image generated using clustering to extract the tissue region, followed by dimensionality reduction. (b) Optical image representative image generated from deep learning classifications. (c) Representative images used to perform multimodal registration to find a mapping aligning the data sets. (d) Validated on a range of MSI modalities (DESI, MALDI, and IR-REIMS) across a range of pixel sizes (15–100 μm). Shown are three examples, with the representative images overlaid onto the histology data. Validation data sets are summarized in the plot (right), showing the mean Hausdorff distance calculated,³⁸ with dashed lines indicating multiples of the expected minimum distance (see the Supporting Information for more details).

First, as the authors note, the “background” regions of MSI images (non-tissue regions, such as the substrate, embedding medium, or the so called “halo” effect in MSI) can affect the registration success and so should be removed but provide no methodology for performing this automatically. Second, for large data sets, t-SNE can be prohibitively time-consuming. To address these shortcomings, and to make use of the additional information available from the deep learning model, we propose a new registration process, as shown in Figure 2. Here, the classifications from the deep learning model are used as a representative image for the histology data as they represent areas of biological difference that are likely to be visible in the MSI data (through one or more ion images).

For the MSI data, unsupervised clustering is employed to isolate the tissue region, followed by dimensionality reduction. A comparison of 3D reduction methods, t-SNE (as used in the work by Abdelmoula et al.³⁷), UMAP,³¹ and Ivis,³² was performed (Figures S2–S4). For this relatively small data set (7777 pixels), t-SNE takes 419 s, compared to 50 s for Ivis and 23 s for UMAP. When scaling this up to a data set consisting of 123,557 pixels (representing approximately a 4 \times reduction in pixel size, from 80 to 20 μm), t-SNE requires over an hour, whereas Ivis and UMAP require 20 and 5 min, respectively. It is worth noting that all calculations were performed using a CPU. As Ivis is based on TensorFlow, use of a GPU will provide significant improvements in timings compared to those presented here.

A comparison of the embedded data (when reducing to three dimensions) for each of the 3D reduction techniques (Figures S2–S4) shows that regardless of the means of converting the three dimensions to a grayscale image for use in the registration process (either directly to RGB or by using CIE $L^*a^*b^*$ as an intermediary), visibly separable features in the color image are no longer separable in the grayscale image. In some cases, this masks features comparable to those in the

H&E classifications and can result in poor alignment, as seen in the third validation data set (see Supporting Information, Table S3 and Figure S6).

In contrast, reducing to a single dimension directly results in features comparable with the H&E classifications (visible in the example, as shown in Figure 2). Both t-SNE and UMAP produce comparable results (see “Validation” discussion in Supporting Information and Figure S5 and Tables S1–S4), regardless of the normalization applied (although the exact intensity values for each region differ, the same features can be seen in both representations); however, Ivis performs poorly in the 1D case. The order of magnitude reduction in speed between t-SNE and UMAP, for equivalent results, facilitates the use of such a workflow routinely.

The registration workflow was further evaluated on a range of MSI modalities (DESI, IR-REIMS, and MALDI, as shown in Figure 2d) acquired with a range of pixel sizes (15–100 μm). The most significant determinant of the accuracy of the registration process was the quality of the MSI data (and not necessarily the pixel size in isolation), with high-quality data (in terms of spatial resolution, clearly defined features in the sample) approaching the minimum expected value for the Hausdorff distance used to evaluate registration accuracy (depicted as the lowest dashed line in the plot in Figure 2d). More details and discussion on the registration validation can be found in the Supporting Information.

The most common output following image registration is the visualization of MSI data either alongside or as an overlay on top of a H&E image. This has been used in many studies to interpret molecular distribution in the context of pathology, for example, in drug distribution studies.³⁹ The workflow presented above also enables this to be performed (as demonstrated by displaying the dimensionality-reduced MSI data on the histology data in Figure 2c) but also enables deeper integration of the two modalities, as discussed below.

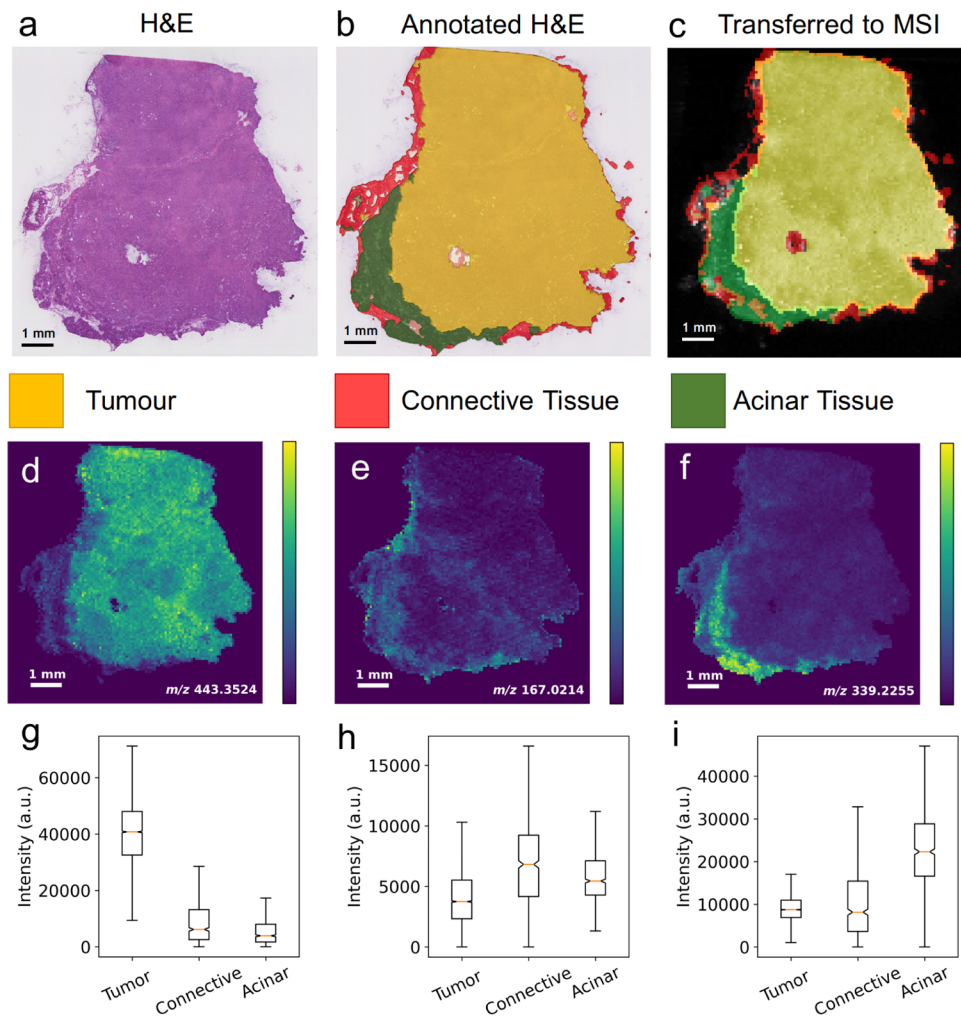


Figure 3. Demonstration of annotations transferred from H&E to MSI data. The transferred annotations were subsequently used to find ion images, which correlate with each annotation, and then region-specific statistics were generated. (a) H&E image. (b) Annotations as determined using the deep learning model. (c) Deep learning annotations transferred to MSI. (d–f) Ion image which highly correlates with each of the transferred deep learning annotations; tumor (d, m/z 443.3524), connective tissue (e, m/z 167.0214), and acinar tissue (f, m/z 339.2255), respectively. Ion image with the highest Pearson's correlation shown with ± 3 PPM. (g–i) Intensities (ion counts) from each region for ion images shown in (d–f).

Annotation Transfer. Once the data sets are linked by the registration transform, it is possible to translate any coordinate from one modality to the other. The annotation transfer workflow is shown in Figure 1 and is agnostic to both the means of generating annotations and the registration workflow used. This means that any future improvements made in the field of multimodal registration, or indeed any existing registration workflow proposed by the community,^{9,37} can be integrated into the annotation transfer workflow by simply exchanging the registration step.

From H&E to MSI. Annotation files generated by marking regions on histology images, by either trained pathologists (using digital pathology software) or automated annotation tools (increasingly based on neural networks), consist of points (x, y coordinate pairs) in the histology image space which when joined together form the outline of an annotated region. A single annotation, such as “tumor”, can comprise multiple regions, some of which could be “negative” regions (i.e., regions which form a hole in another region). This is visible in the H&E data, as shown in Figure 3, where a large region marked as “tumor” (yellow) also contains multiple holes.

The most common way to transfer annotations is to use an image representation of each annotation, where the annotation image is the same size as the histology image, and each pixel which makes up the edge of the annotation is given a specific color.¹⁰ The registration transform is then applied to this annotation image to provide annotations in the MSI space. As this requires an annotation image of equal size to the histology image, this can be both memory and computationally expensive. An alternative method is to manually copy the annotation to the MSI space; however, this is time-consuming (approximately 20 min per section with the three annotations visible in Figure 3b) and prone to human error. In contrast, applying the registration transform to each of the data points in the annotation file is computationally and memory efficient (less than a second for the three annotations visible in Figure 3b). Visualization of the H&E annotations transferred to the MSI data using SpectralAnalysis is shown in Figure 3b,c.²¹

As the pixel size of the MSI data is significantly larger than that of the H&E image, it is not uncommon that multiple points making up a given histology annotation fall within the same MSI pixel when transformed to the MSI space. These

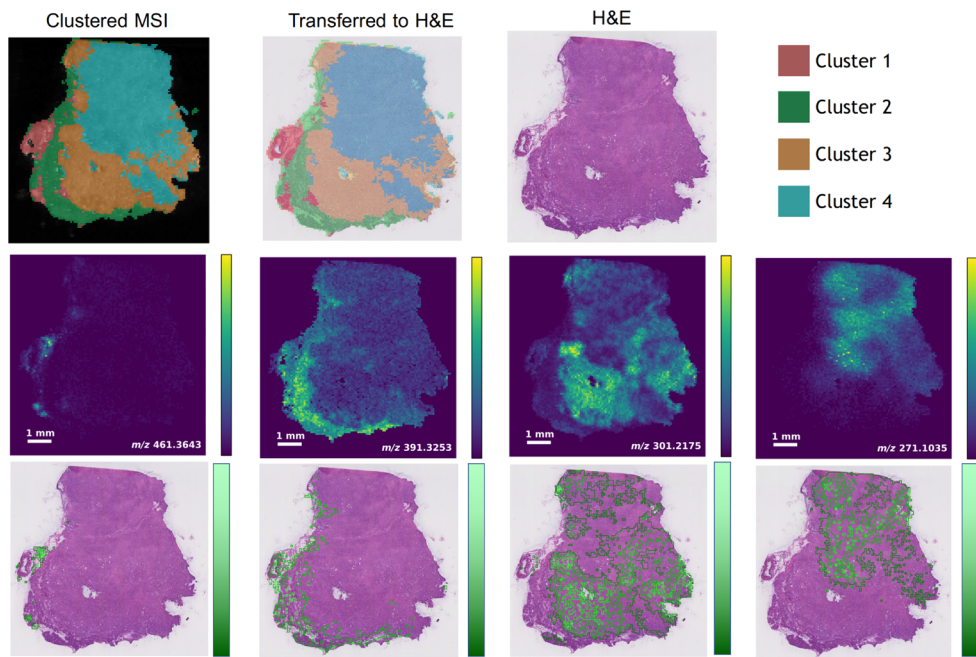


Figure 4. (First row) Clustering applied to MSI data. (Second row) Ion images which correlate with each cluster, 1–4 (generated using SpectralAnalysis²¹). (Third row) Ion images converted to a contour map and transferred to H&E annotations and visualized in digital pathology software (ImageScope), where annotations correspond to thresholds set for >0, >20, >40, >60, and >80%, with each increasing bright shade of green.

points could originate from multiple annotations, resulting in a single MSI pixel with multiple labels. There are multiple options for dealing with this: (1) assign the pixel to all labels which cover some portion of the pixel, (2) assign the pixel to the label which covers the largest area, (3) assign the pixel to all labels but assign weights to each pixel corresponding to the relative area covered by each annotation, (4) assign no label to any pixel which has multiple candidate labels, or (5) create a new label to describe the combination of all candidate labels.

The choice of which option to pursue is dependent on the desired outcome and the algorithm being used. In some cases, it may be desirable to omit pixels which cover multiple labels. For example, when training a classifier, the inclusion of pixels which cover multiple anatomical regions could corrupt the classifier and reduce the performance. It may, in this situation, be of interest to include these pixels in a new, separate, label (i.e., option 5), a combination of the contributing labels. This may then more accurately describe boundaries between labels, for example, tumor margin regions.

Once histological annotations have been transferred to the MSI space, one way of using these is to find ion images which correlate with each annotated region and extract statistics from the MSI data. The transformed coordinates were converted to a ROI file compatible with SpectralAnalysis.²¹ These ROI files were then used, correlating each ion image with each annotation (top 20 list for each annotation with tentative identifications in Tables S5–S8 with corresponding ion images, as shown in Figures S12–S15), revealing glucose (MS/MS spectrum and comparison to reference, as shown in Figure S11) localized in the connective tissue, ceramides, diglycerides, and other lipids in the acinar tissue and lactate in the tumor region. These annotations were then also used to extract statistics from the ion images using the “Region of Interest Details” tool in Spectral Analysis, as shown in Figure 3g–i.

From MSI to H&E. As it is possible to calculate the inverse transformation, it is also possible to perform the coordinate transformation in reverse, converting MSI pixel coordinates to coordinates in the H&E space. As the MSI pixels are significantly larger than the H&E pixels, there are two ways these coordinates can be represented: (1) the central point from the pixel is transformed and (2) a shape (square in this case) is formed to represent the area analyzed and the shape is then transformed. In the second case, this results in an area that covers the size of the pixel in MSI being translated to the optical image. This is a more accurate representation of MSI data and so is used in this study; however, in other modalities, or for MSI data which have pixel sizes much larger than the probe size, the first option may be the more appropriate choice.

The simplest, but still powerful, way of using the inverse transformation is to present the distribution of a single ion image as an annotation in digital pathology software. This allows investigation of the distribution of ions of interest in the context of the full, high-resolution H&E image data, visualizing the colocalization of metabolites, pharmaceutical compounds, and other biomarkers with tissue morphology. In this example, clustering was applied to the MSI data, and then, ion images which correlate with each cluster were found. To incorporate intensity, multiple annotations were created for a single ion image, representing the ion image thresholded at increasing intensities. This has the effect of generating a contour-like map when all annotations are viewed together. By also coloring each annotation using a color scale and according to the intensity threshold, both the intensity and spatial information can be retained when viewing ion image data in digital pathology software, as shown in Figure 4.

Machine learning techniques, such as the clustering applied above, are being increasingly employed in MSI to handle the high dimensionality and significant data complexity.^{40–42} It is a

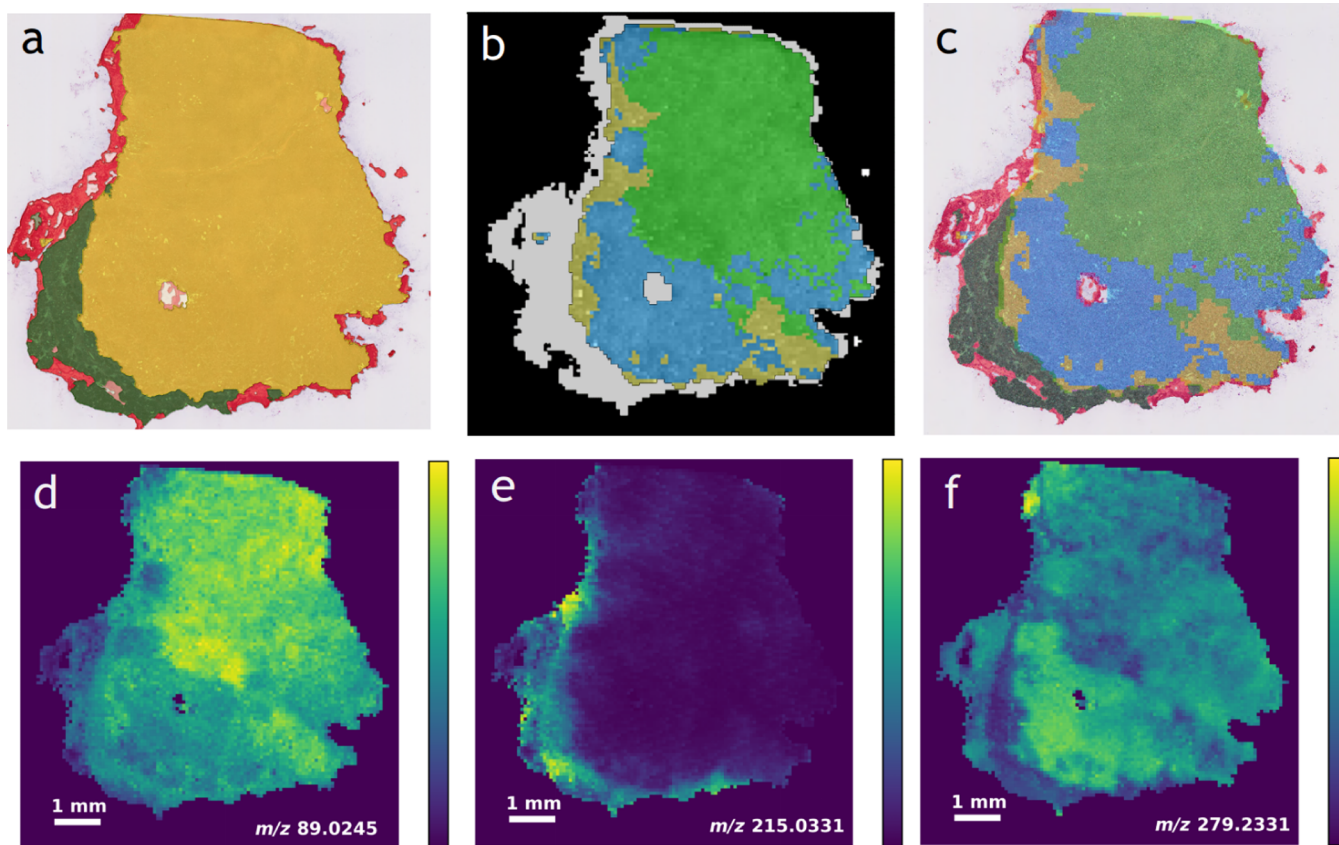


Figure 5. The tumor region of MSI data was extracted using an annotation generated using deep learning from H&E data and transferred to the MSI space. (a) Annotations as determined by the deep learning model (red represents connective tissue, green represents acinar tissue, and yellow represents tumor). (b) Clustering applied to the tumor only spectra (resulting in yellow, green, and blue regions). Non-tumor, on-tissue spectra shown in gray but were not included in the clustering. (c) Transferred cluster regions from the MSI tumor region displayed alongside non-tumor annotations generated by the deep learning model. (d) m/z 89.0245 tentatively identified as lactate $[M - H]^-$. (e) m/z 215.0331, a hexose (tentatively identified as glucose $[M + Cl]^-$ based on MS/MS and the well-documented high glucose content in cancer tissues due to their dramatically increased glycolytic flux⁴³). (f) m/z 279.2331 tentatively identified as FA(18:2) $[M - H]^-$.

common desire to be able to relate the results of such analysis back to H&E data. It is also possible to transform the output from machine learning algorithms (such as clustering) to the H&E space, as shown in Figure 5.

To better understand tumor heterogeneity in the PDAC samples, the transferred tumor annotation (generated using deep learning classification) was used to extract only spectra relating to the tumor region from the MSI data. Clustering was then applied to the tumor subset of data to reveal metabolically different regions in the data. This enabled identification and stratification of cellular populations and phenotypes from the TME based on characteristic metabolic fingerprint of each region by correlating each ion image with each cluster (top 20 list for each cluster with tentative identifications in Tables S5–S8 with corresponding ion images, as shown in Figures S12–S15). It is well described that an extensive metabolic rewiring due to both mutations and tissue remodeling appears in PDAC involving the rise of two main cell populations; cancer-associated fibroblasts and tumor cells.⁴⁴ The latter population can be further divided into hypoxic and normoxic tumor cells.⁴⁵ Hypoxic cells avidly uptake glucose, degraded through glycolysis to give lactate and ATP, and use glutamine through glutaminolysis to gain biomass and redox power. Consequently, adjacent normoxic cells use lactate to proliferate (tumor symbiosis). Moreover, the TME of PDAC is known to be highly immunosuppressive, and adenosine signaling has

emerged as a key metabolic pathway, regulating this tumor immunity.⁴⁶ Fatty acids drive inflammatory response within the tissue depending on their chain length and unsaturation number, which range from saturated fatty acids (SFAs) to mono and poly unsaturated fatty acids (MUFAs and PUFAs).⁴⁷ For example, PUFAs promote the production of anti-inflammatory cytokines, while SFAs limit their production and support the synthesis of pro-inflammatory cytokines.⁴⁸

The core cluster (green, as shown in Figure 5b) displays a high lactate accumulation with comparatively low glucose levels, suggesting a highly glycolytic environment, as would be expected from hypoxic cells. PUFAs [FA(16:2), FA(18:2), FA(20:5), FA(22:5), and FA(22:6)] are preferentially located within the blue cluster, which can indicate a lower inflammatory response in this region of the tumor. Within the yellow cluster, glucose was readily detected, while FA(18:2) was lower than the other clusters, indicating a less hypoxic or tumor margin region.

The MSI clusters were then transferred to the H&E space to investigate potential histological differences between the metabolically unique regions, as shown in Figure 5. The blue and green clusters consisted of a neoplastic tissue with no obvious histopathological differences observable between the two. The yellow cluster comprised acinar-to-ductal metaplasia, with variable infiltration of neoplastic epithelial cells. This supports the finding mentioned above, suggesting that this

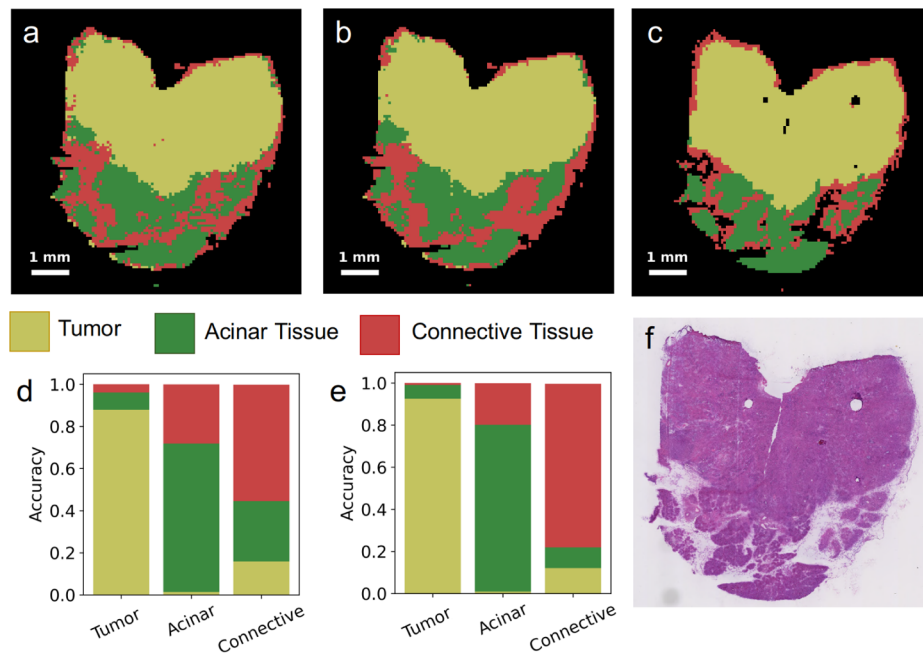


Figure 6. Using annotations generated from the H&E deep learning model to train a classifier for distinguishing tumor, acinar tissue, and connective tissue. The classifier was trained on data, as shown in Figure 3. (a) Classification result when using all deep learning pathology annotations transferred to MSI space. (b) Classification result when removing pixels which have multiple annotation labels from the training set. (c) Deep learning pathology annotations transferred to MSI. (d) Stacked bar chart comparing (a,c). (e) Stacked bar chart comparing (b,c). (f) H&E image used to generate deep learning annotations from (c).

cluster corresponds to a tumor margin region. Further investigation of this could be performed through the use of single-cell morphologic analysis.⁴⁹

Enabling Additional Workflows. The ability to transfer annotations or labels from one modality to another also enables additional workflows and means of interrogating the data to be easily performed. One such example is building a classifier for one data set based on the annotations determined using the other. The labels transferred from the annotated histology were used to build a classifier for the MSI data. In this case, the annotated pixels from the data presented in Figure 3 were used as an input to a KNN classifier (using option 1, described above for handling multiple labels per pixel, resulting in a class error of 0.11). Data acquired from a second mouse were then classified using the learnt model, whose results are shown in Figure 6a. These classifications were then compared to annotations generated using the deep learning H&E model (and subsequently transferred to the MSI space, Figure 6c), as shown in Figure 6d and in table form in Table 1 (top). Agreement between the classifier and the transferred H&E annotations was 87, 70, and 55% for tumor, acinar tissue, and connective tissue, respectively. It is not unexpected that there are differences as MSI and H&E measure different aspects of the sample at different resolutions.

Repeating the process with overlapping annotations removed from the classification model (option 4 for handling multiple labels per pixel, resulting in a class error of 0.0398), agreement between the two modalities is increased significantly (Figure 6b,e and Table 1 bottom) with tumor regions agreement increased to 92%, acinar tissue to 79%, and connective tissue to 77%. The improved classification accuracy indicates that DESI pixels with multiple annotations are metabolically different from those with a single classification,

Table 1. Comparison of Methods for Handling Overlapping Annotations When Transferring from High to Low Spatial Resolution When Building a Classifier^a

method	region	tumor	acinar tissue	connective tissue
all	tumor	0.8790	0.0817	0.0393
all	acinar tissue	0.0141	0.7046	0.2806
all	connective tissue	0.1588	0.2864	0.5531
unique	tumor	0.9253	0.0652	0.0095
unique	acinar tissue	0.0092	0.7919	0.1976
unique	connective tissue	0.1205	0.0990	0.7768

^aMethod all: each pixel maintains all annotations. Method unique: only pixels which have a unique annotation are included in the classifier. Agreement between KNN classifier trained on MSI data and deep learning pathology annotations transferred to the MSI data space is shown.

likely due to the fact that they represent the margin region between two classes.

To handle margin regions more explicitly, it is possible to add in new labels for the overlapping regions (option 5 for handling multiple labels per pixel, resulting in a class error of 0.11). The results of the classification applied to the second data set are shown in Figure S16. While this shows promise in successfully annotating boundary regions between annotations, not every boundary is labeled with a boundary label. This is likely due to the limited number of spectra in the original data set which forms each boundary region, limiting the ability of the classifier.

CONCLUSIONS

The workflow presented here used multimodal registration to enable the transfer of annotations from one modality to another, and back again, to enable multimodal data integration. The output of a deep learning model used to annotate the

tumor region of histology data was transferred to MSI data to extract tumor region-specific mass spectra. Clustering these spectra revealed regions of heterogeneity which could then be associated with different metabolic processes in the TME. Transfer of the clusters back to H&E enabled investigation of the metabolically unique regions using digital pathology software. This bidirectional annotation transfer provides a means of multimodal data integration and a route to better understand tumor heterogeneity, which improves on interpretation of any technique in isolation.

As the proposed workflow is technique agnostic, it is possible to integrate further data, such as additional immunohistochemistry-stained images to visualize immune cells to confirm the hypothesis derived from the MSI data or IMC data to visualize structural and functional proteins simultaneously.

The automated integration of histology, deep learning, and spatially resolved metabolomics also enables new workflows to be easily performed. This could include data acquisition using high-resolution imaging experiments based on deep learning classifications, probe techniques such as LESA for localized extraction and mass spectrometry analysis, and laser capture microdissection systems to extract unique regions based on both H&E and MSI information for proteomics and transcriptomics experiments. This deeper integration of spatially resolved metabolomics and histology may also pave the way to reducing the human variability present in the current gold standard for annotating biological samples, where different pathologists can provide conflicting assessments, through the addition of metabolic information. An additional use of such transferred histology-based annotations could be to accurately normalize MSI data. Matrix effects, affecting ionization and suppression in MSI, have been shown to be dependent on anatomical regions.⁵⁰

ASSOCIATED CONTENT

Supporting Information

The Supporting Information is available free of charge at <https://pubs.acs.org/doi/10.1021/acs.analchem.0c02726>.

Annotation transfer, H&E images for each classification and cluster, ion images and corresponding tentative identifications for top 20 ion images which correlate with each cluster, and validation of the registration process through comparison to literature ([PDF](#))

AUTHOR INFORMATION

Corresponding Author

Alan M. Race – *Imaging and AI, Clinical Pharmacology and Safety Sciences, BioPharmaceuticals R&D, AstraZeneca, Cambridge CB4 0WG, U.K.;* [ORCID iD](https://orcid.org/0000-0001-8962-2641); Phone: +49 (0)6421 28-65797; Email: alan.race@uni-marburg.de; Fax: +49 (0)6421 28-68921

Authors

Daniel Sutton – *Imaging and AI, Clinical Pharmacology and Safety Sciences, BioPharmaceuticals R&D, AstraZeneca, Cambridge CB4 0WG, U.K.*

Gregory Hamm – *Imaging and AI, Clinical Pharmacology and Safety Sciences, BioPharmaceuticals R&D, AstraZeneca, Cambridge CB4 0WG, U.K.*

Gareth Maglennon – *Oncology Safety, Clinical Pharmacology and Safety Sciences, BioPharmaceuticals R&D, AstraZeneca, Cambridge CB4 0WG, U.K.*

Jennifer P. Morton – *Cancer Research UK Beatson Institute, Glasgow G61 1BD, U.K.; Institute of Cancer Sciences, University of Glasgow, Glasgow G61 1QH, U.K.*

Nicole Strittmatter – *Imaging and AI, Clinical Pharmacology and Safety Sciences, BioPharmaceuticals R&D, AstraZeneca, Cambridge CB4 0WG, U.K.;* [ORCID iD](https://orcid.org/0000-0003-1277-9608)

Andrew Campbell – *Cancer Research UK Beatson Institute, Glasgow G61 1BD, U.K.*

Owen J. Sansom – *Cancer Research UK Beatson Institute, Glasgow G61 1BD, U.K.; Institute of Cancer Sciences, University of Glasgow, Glasgow G61 1QH, U.K.*

Yinhai Wang – *Discovery Sciences, R&D, AstraZeneca, Cambridge CB4 0WG, U.K.*

Simon T. Barry – *Bioscience, Early Oncology, AstraZeneca, Cambridge CB4 0WG, U.K.*

Zoltan Takáts – *Department of Surgery and Cancer, Imperial College London, London SW7 2AZ, U.K.;* [ORCID iD](https://orcid.org/0000-0002-0795-3467)

Richard J. A. Goodwin – *Imaging and AI, Clinical Pharmacology and Safety Sciences, BioPharmaceuticals R&D, AstraZeneca, Cambridge CB4 0WG, U.K.; Institute of Infection, Immunity and Inflammation, College of Medical, Veterinary and Life Sciences, University of Glasgow, Glasgow G12 8QQ, U.K.*

Josephine Bunch – *Department of Surgery and Cancer, Imperial College London, London SW7 2AZ, U.K.; National Centre of Excellence in Mass Spectrometry Imaging (NiCE-MSI), National Physical Laboratory, Teddington TW11 0LW, U.K.*

Complete contact information is available at:
<https://pubs.acs.org/10.1021/acs.analchem.0c02726>

Notes

The authors declare the following competing financial interest(s): D.S., G.H., G.M., N.S., Y.W., S.T.B and R.J.A.G. are employees and shareholders of AstraZeneca. A.M.R. is a fellow in the AstraZeneca postdoctoral program.

ACKNOWLEDGMENTS

The authors wish to thank the wider Cancer Research UK Grand Challenge Rosetta Consortium members for supporting this research. They would also like to thank the Biological Services Unit at the CRUK Beatson Institute. The authors gratefully acknowledge funding from Cancer Research UK (A24034, A25142, A17196, A21139, and A25233) which supported this work.

REFERENCES

- (1) Fass, L. *Mol. Oncol.* **2008**, *2*, 115–152.
- (2) Holzlechner, M.; Eugenin, E.; Prideaux, B. *Cancer Rep.* **2019**, *2*, No. e1229.
- (3) Goodwin, R. J. A.; Bunch, J.; McGinnity, D. F. *Adv. Cancer Res.* **2017**, *134*, 133–171.
- (4) Schwamborn, K. *Adv. Cancer Res.* **2017**, *134*, 1–26.
- (5) Chaurand, P.; Schwartz, S. A.; Billheimer, D.; Xu, B. J.; Crecelius, A.; Caprioli, R. M. *Anal. Chem.* **2004**, *76*, 1145–1155.
- (6) Eberlin, L. S.; Ferreira, C. R.; Dill, A. L.; Ifa, D. R.; Cheng, L.; Cooks, R. G. *ChemBioChem* **2011**, *12*, 2129–2132.

- (7) Abdelmoula, W. M.; Škrášková, K.; Balluff, B.; Carreira, R. J.; Tolner, E. A.; Lelieveldt, B. P. F.; van der Maaten, L.; Morreau, H.; van den Maagdenberg, A. M. J. M.; Heeren, R. M. A.; McDonnell, L. A.; Dijkstra, J. *Anal. Chem.* **2014**, *86*, 9204–9211.
- (8) Patterson, N. H.; Tuck, M.; Van De Plas, R.; Caprioli, R. M. *Anal. Chem.* **2018**, *90*, 12395–12403.
- (9) Patterson, N. H.; Tuck, M.; Lewis, A.; Kaushansky, A.; Norris, J. L.; Van De Plas, R.; Caprioli, R. M. *Anal. Chem.* **2018**, *90*, 12404–12413.
- (10) Heijs, B.; Abdelmoula, W. M.; Lou, S.; Briaire-de Brujin, I. H.; Dijkstra, J.; Bovée, J. V. M. G.; McDonnell, L. A. *Anal. Chem.* **2015**, *87*, 11978–11983.
- (11) Verbeeck, N.; Yang, J.; De Moor, B.; Caprioli, R. M.; Waelkens, E.; Van de Plas, R. *Anal. Chem.* **2014**, *86*, 8974–8982.
- (12) Dewez, F.; Martin-Lorenzo, M.; Herfs, M.; Baiwir, D.; Mazzucchelli, G.; De Pauw, E.; Heeren, R. M. A.; Balluff, B. *Anal. Bioanal. Chem.* **2019**, *411*, 5647–5653.
- (13) Bychkov, D.; Linder, N.; Turkki, R.; Nordling, S.; Kovanen, P. E.; Verrill, C.; Wallander, M.; Lundin, M.; Haglund, C.; Lundin, J. *Sci. Rep.* **2018**, *8*, 3395.
- (14) Long, J.; Shelhamer, E.; Darrell, T. Fully convolutional networks for semantic segmentation. *2015 IEEE Conference on Computer Vision and Pattern Recognition*, 2015; pp 3431–3440.
- (15) Ronneberger, O.; Fischer, P.; Brox, T. U-net: Convolutional networks for biomedical image segmentation. *International Conference on Medical Image Computing and Computer-Assisted Intervention*; Springer, 2015; Vol. 9351, pp 234–241.
- (16) Hingorani, S. R.; Wang, L.; Multani, A. S.; Combs, C.; Deramaudt, T. B.; Hruban, R. H.; Rustgi, A. K.; Chang, S.; Tuveson, D. A. *Cancer Cell* **2005**, *7*, 469–483.
- (17) Dannhorn, A.; Kazanc, E.; Ling, S.; Nikula, C.; Karali, E.; Serra, M. P.; Vorng, J.-L.; Inglese, P.; Maglennan, G.; Hamm, G.; Swales, J.; Strittmatter, N.; Barry, S. T.; Sansom, O. J.; Poulogiannis, G.; Bunch, J.; Goodwin, R. J.; Takats, Z. *Anal. Chem.* **2020**, *92*, 11080–11088.
- (18) Abbassi-Ghadi, N.; Jones, E. A.; Veselkov, K. A.; Huang, J.; Kumar, S.; Strittmatter, N.; Golf, O.; Kudo, H.; Goldin, R. D.; Hanna, G. B.; Takats, Z. *Anal. Methods* **2015**, *7*, 71–80.
- (19) Chambers, M. C.; Maclean, B.; Burke, R.; Amodei, D.; Ruderman, D. L.; Neumann, S.; Gatto, L.; Fischer, B.; Pratt, B.; Egertson, J.; Hoff, K.; Kessner, D.; Tasman, N.; Shulman, N.; Frewen, B.; Baker, T. A.; Brusniak, M.-Y.; Paulse, C.; Creasy, D.; Flashner, L.; Kani, K.; Moulding, C.; Seymour, S. L.; Nuwaysir, L. M.; Lefebvre, B.; Kuhlmann, F.; Roark, J.; Rainer, P.; Detlev, S.; Hemenway, T.; Huhmer, A.; Langridge, J.; Connolly, B.; Chadick, T.; Holly, K.; Eckels, J.; Deutsch, E. W.; Moritz, R. L.; Katz, J. E.; Agus, D. B.; MacCoss, M.; Tabb, D. L.; Mallick, P. *Nat. Biotechnol.* **2012**, *30*, 918–920.
- (20) Race, A. M.; Styles, I. B.; Bunch, J. *J. Proteomics* **2012**, *75*, 5111–5112.
- (21) Race, A. M.; Palmer, A. D.; Dexter, A.; Steven, R. T.; Styles, I. B.; Bunch, J. *Anal. Chem.* **2016**, *88*, 9451–9458.
- (22) Wishart, D. S.; Feunang, Y. D.; Marcu, A.; Guo, A. C.; Liang, K.; Vázquez-Fresno, R.; Sajed, T.; Johnson, D.; Li, C.; Karu, N.; Sayeeda, Z.; Lo, E.; Assempon, N.; Berjanskii, M.; Singhal, S.; Arndt, D.; Liang, Y.; Badran, H.; Grant, J.; Serra-Cayuela, A.; Liu, Y.; Mandal, R.; Neveu, V.; Pon, A.; Knox, C.; Wilson, M.; Manach, C.; Scalbert, A. *Nucleic Acids Res.* **2018**, *46*, D608–D617.
- (23) Smith, C. A.; Maille, G. O.; Want, E. J.; Qin, C.; Trauger, S. A.; Brandon, T. R.; Custodio, D. E.; Abagyan, R.; Siuzdak, G. *Ther. Drug Monit.* **2005**, *27*, 747–751.
- (24) Fahy, E.; Subramaniam, S.; Murphy, R. C.; Nishijima, M.; Raetz, C. R. H.; Shimizu, T.; Spener, F.; van Meer, G.; Wakelam, M. J. O.; Dennis, E. A. *J. Lipid Res.* **2009**, *50*, S9–S14.
- (25) Sanchez, D.; Cheung, W. L. *Transl. Cancer Res.* **2015**, *4*, 608–615.
- (26) Deng, J.; Dong, W.; Socher, R.; Li, L.-J.; Kai, L.; Li, F.-F. ImageNet: A large-scale hierarchical image database. *2009 IEEE Conference on Computer Vision and Pattern Recognition*, 2009; pp 248–255.
- (27) Huang, G.; Liu, Z.; Van Der Maaten, L.; Weinberger, K. Q. Densely connected convolutional networks. *Proceedings—30th IEEE Conference on Computer Vision and Pattern Recognition, CVPR 2017*, 2017; pp 2261–2269.
- (28) Race, A. M.; Bunch, J. *Anal. Bioanal. Chem.* **2015**, *407*, 2047–2054.
- (29) Van Der Maaten, L. J. P.; Hinton, G. E. *J. Mach. Learn. Res.* **2008**, *9*, 2579–2605.
- (30) Varoquaux, G.; Buitinck, L.; Louppe, G.; Grisel, O.; Pedregosa, F.; Mueller, A. *GetMobile Mob. Comput. Commun.* **2015**, *19*, 29–33.
- (31) McInnes, L.; Healy, J.; Melville, J. UMAP: Uniform Manifold Approximation and Projection for Dimension Reduction. 2018, arXiv:1802.03426. <http://arxiv.org/abs/1802.03426>.
- (32) Szubert, B.; Cole, J. E.; Monaco, C.; Drozdov, I. *Sci. Rep.* **2019**, *9*, 8914.
- (33) Klein, S.; Staring, M.; Murphy, K.; Viergever, M. A.; Pluim, J. *IEEE Trans. Med. Imag.* **2010**, *29*, 196–205.
- (34) Esteva, A.; Kuprel, B.; Novoa, R. A.; Ko, J.; Swetter, S. M.; Blau, H. M.; Thrun, S. *Nature* **2017**, *542*, 115–118.
- (35) Khan, S.; Islam, N.; Jan, Z.; Ud Din, I.; Rodrigues, J. J. P. C. *Pattern Recognit. Lett.* **2019**, *125*, 1–6.
- (36) Chughtai, K.; Jiang, L.; Greenwood, T. R.; Klinkert, I.; Amstalden van Hove, E. R.; Heeren, R. M. A.; Glunde, K. *Anal. Chem.* **2012**, *84*, 1817–1823.
- (37) Abdelmoula, W. M.; Carreira, R. J.; Shyti, R.; Balluff, B.; Van Zeijl, R. J. M.; Tolner, E. A.; Lelieveldt, B. P. F.; Van Den Maagdenberg, A. M. J. M.; McDonnell, L. A.; Dijkstra, J. *Anal. Chem.* **2014**, *86*, 3947–3954.
- (38) Taha, A. A.; Hanbury, A. *IEEE Trans. Pattern Anal. Mach. Intell.* **2015**, *37*, 2153–2163.
- (39) Hamm, G. R.; Bäckström, E.; Brülls, M.; Nilsson, A.; Strittmatter, N.; Andrén, P. E.; Grime, K.; Fridén, M.; Goodwin, R. J. A. *J. Aerosol Med. Pulm. Drug Delivery* **2020**, *33*, 43–53.
- (40) Verbeeck, N.; Caprioli, R. M.; Van de Plas, R. *Mass Spectrom. Rev.* **2020**, *39*, 245–291.
- (41) Nampei, M.; Horikawa, M.; Ishizu, K.; Yamazaki, F.; Yamada, H.; Kahyo, T.; Setou, M. *Sci. Rep.* **2019**, *9*, 13213.
- (42) Dexter, A.; Race, A. M.; Steven, R. T.; Barnes, J. R.; Hulme, H.; Goodwin, R. J. A.; Styles, I. B.; Bunch, J. *Anal. Chem.* **2017**, *89*, 11293–11300.
- (43) Yan, L.; Raj, P.; Yao, W.; Ying, H. *Cancers* **2019**, *11*, 1460.
- (44) Sousa, C. M.; Biancur, D. E.; Wang, X.; Halbrook, C. J.; Sherman, M. H.; Zhang, L.; Kremer, D.; Hwang, R. F.; Witkiewicz, A. K.; Ying, H.; Asara, J. M.; Evans, R. M.; Cantley, L. C.; Lyssiotis, C. A.; Kimmelman, A. C. *Nature* **2016**, *536*, 479–483.
- (45) Sousa, C. M.; Kimmelman, A. C. *Carcinogenesis* **2014**, *35*, 1441–1450.
- (46) Maj, T.; Wang, W.; Crespo, J.; Zhang, H.; Wang, W.; Wei, S.; Zhao, L.; Vatan, L.; Shao, I.; Szeliga, W.; Lyssiotis, C.; Liu, J. R.; Kryczek, I.; Zou, W. *Nat. Immunol.* **2017**, *18*, 1332–1341.
- (47) O'Neill, L. A. J.; Kishton, R. J.; Rathmell, J. *Nat. Rev. Immunol.* **2016**, *16*, 553–565.
- (48) Zielinski, C. E.; Mele, F.; Aschenbrenner, D.; Jarrossay, D.; Ronchi, F.; Gattorno, M.; Monticelli, S.; Lanzavecchia, A.; Sallusto, F. *Nature* **2012**, *484*, 514–518.
- (49) Ščupáková, K.; Dewez, F.; Walch, A. K.; Heeren, R. M. A.; Balluff, B. *Angew. Chem., Int. Ed.* **2020**, *59*, 17447–17450.
- (50) Taylor, A. J.; Dexter, A.; Bunch, J. *Anal. Chem.* **2018**, *90*, 5637–5645.